Carbon 152 (2019) 497–502

Contents lists available at ScienceDirect

Carbon

journal homepage: www.elsevier.com/locate/carbon

Robust nanocomposites of α-Fe_2O_3 and N-doped graphene oxide: Interfacial bonding and chemisorption of H_2O

Jonathan M. Polfus [a, *], Kaushik Jayasayee [b]

[a] SINTEF Industry, Sustainable Energy Technology, PO Box 124 Blindern, NO-0314, Oslo, Norway
[b] SINTEF Industry, Sustainable Energy Technology, PO Box 4760 Sluppen, NO-7465, Trondheim, Norway

ARTICLE INFO

Article history:
Received 22 March 2019
Received in revised form
10 May 2019
Accepted 14 May 2019
Available online 16 May 2019

ABSTRACT

Nanocomposites of α-Fe_2O_3 (hematite) and (N-doped) graphene oxide (GO) were investigated using first-principles calculations with focus on structure, chemical bonding, electronic structure and H_2O adsorption. The nanocomposites were modeled as the interface between the α-Fe_2O_3 (0 0 0 1) surface and the basal plane of reduced graphene oxide, comprising epoxy groups (C:O ratio of 8) as well as graphitic and pyridinic nitrogen doping. The composite structures exhibited strong chemical bonding by the formation of a bridging Fe–O–C bond. The calculated binding energy between the materials was −0.56 eV per Fe–O–C bond for GO and up to −1.14 eV for N-doped GO, and the binding energies were found to correlate with the charge of the bridging oxide ion. The composites exhibited partly occupied carbon states close to or above the α-Fe_2O_3 valence band maximum. Dissociative adsorption of H_2O was found to be more exothermic for the composites compared to the individual materials, ranging from about −0.9 to −1.7 eV for the most stable configurations with hydroxide species adsorbed to GO and protons forming NH groups or adsorbed to the α-Fe_2O_3 surface.

1. Introduction

Synergistic combinations of the functional properties of metal oxides and graphitic materials have shown great promise for a range of applications including photocatalysts, supercapacitors, batteries and gas sensors [1–4]. For instance, the improved performance of photocatalysts comprising an oxide semiconductor and graphene oxide (GO) has been ascribed to longer charge carrier lifetime as photogenerated electrons are injected into GO. In addition, functionalized GO can provide catalytically active sites for, e.g., water splitting and CO_2 reduction [5,6]. Similarly, graphene oxide has been used as a conductive network in quantum dot sensitized solar cells [7]. In the case of hybrid supercapacitors, pseudocapacitive transition metal oxides such as MnO_2 and Fe_2O_3/Fe_3O_4 provide high energy density while graphene-based materials provide electrochemical double-layer capacitance with fast response times, while also serving as a conductive network [8–11]. Furthermore, composites can also retain the microstructure and high surface area of the constituents by mitigating both agglomeration of oxide nanoparticles and stacking of the graphitic materials.

Nanocomposites between α-Fe_2O_3 and GO have been applied as photocatalyst, [12] electrode material for supercapacitors, [13–16] sensors, [17–20] lithium-ion and sodium-ion batteries, [21,22] and lubrication additive [23]. The functional properties of the nanocomposites can be expected to depend on the interface between the materials, which is inherently challenging to accurately characterize in terms of chemical bonding, electronic structure and electrochemical properties. The mechanisms for enhanced performance are often uncertain due to the complexity of the nanocomposite material systems. Moreover, it is necessary to identify robust composite structures with sufficient thermal and chemical stability for application in devices.

GO can contain a variety of non-ordered functional groups and epoxy, hydroxyl and carbonyl are the main groups on the basal plane [24,25]. Improved electronic conductivity can be achieved by thermal or chemical reduction to obtain C:O atomic ratios in the range of about 5–15 [26]. Doping of graphene and GO with nitrogen has been utilized to modulate the electronic properties of the material and to increase the number of catalytically active sites – at nitrogen or adjacent carbon atoms with altered charge density [27,28]. Nitrogen can be doped into several bonding configurations in the basal plane or at the edges of graphene, and there is much debate surrounding the type of nitrogen species that contribute to

* Corresponding author.
E-mail address: jonathan.polfus@sintef.no (J.M. Polfus).

https://doi.org/10.1016/j.carbon.2019.05.033

the enhanced functional properties. We focus on two of the most common substitutions: quaternary N which substitutes C in the graphene lattice, denoted graphitic N, and pyridinic N which can form on graphene edges or within the basal plane as a cluster comprising a C vacancy surrounded by three quaternary N. In both cases, sp^2 hybridization is retained for pristine graphene, while the hybridization depends on the local structural configuration of the functional groups in the case of GO. Nitrogen may be doped into the oxide part of the nanocomposite as well and it has been shown that NH^{2-}, which is isoelectronic with the oxide ion, is thermodynamically favored in hydrogen-containing atmospheres in many systems [29].

There are quite few computational studies on interfaces between GO and metal oxides; notable exceptions include graphene/GO heterostructures with α-Fe_2O_3, [30] TiO_2 [31], MgO [32] and (Na,K)NbO_3 [33,34]. However, chemical bonding between the oxide and GO structure has not been considered in most cases. In this respect, it was recently reported that nanocomposites between α-Al_2O_3 (0 0 0 1) and GO with epoxy groups can form strong bridging Al–O–C bonds between the materials [35]. Formation of interfacial Ti–O–C bonds has also been reported for composites between GO and TiO_2 [36]. Furthermore, many applications of these nanocomposites involve an aqueous acidic or alkaline environment, e.g., photocatalysis, proton exchange membrane (PEM) fuel cells or solid-state supercapacitors. It is therefore important to understand how adsorption of H_2O may affect the nanocomposites in terms of changes in the functional groups, catalytic sites and electronic structure.

In the present work, we have further investigated nanocomposites of α-Fe_2O_3 and (N-doped) GO using density functional theory (DFT) calculations. The composite was modelled as an interface between α-Fe_2O_3 (0 0 0 1) and the basal plane of GO with bridging Fe–O–C bonds based on previous work on isostructural α-Al_2O_3 (0 0 0 1) [35]. The model thereby represents a region of the nanocomposite with strong chemical bonding between the materials. The GO structure was doped with graphitic and pyridinic nitrogen, and the influence of doping on the electronic structure and binding energy between the materials was evaluated. Finally, chemisorption of H_2O on the (N-doped) GO and α-Fe_2O_3 surface region was investigated.

2. Computational procedures

Spin-polarized DFT calculations were performed using VASP [37] and the projector-augmented wave (PAW) method [38]. The PBE generalized gradient approximation [39] was employed in combination with the DFT + U approach due to Dudarev et al. [40] An effective on-site Coulomb interaction parameter of $U = 4.3$ eV was chosen for Fe in line with several previous studies [41–43]. The van der Waals forces that are of significant importance for graphene structures were taken into account through the semi-empirical DFT + D2 correction scheme due to Grimme [44]. This approach has been successfully applied for describing geometries of graphene-related structures, [45,46] and interfaces between graphene and metal oxides [32,47–50]. The calculations were performed with a 500 eV plane-wave energy cutoff and k-point sampling according to $8 \times 8 \times 1$ and $16 \times 16 \times 1$ grids for the α-Fe_2O_3 slab and graphene, respectively. The atomic positions were optimized until the residual forces were within 0.02 eV Å^{-1} (0.05 eV Å^{-1} with H_2O adsorbates) and the electronic energy convergence was 10^{-6} eV. The included valence electrons were Fe $3p^6d^6 4s^2$, C $2s^2p^2$, O $2s^2p^4$ and N $2s^2p^3$.

The α-Fe_2O_3 (0 0 0 1) surface was constructed as a symmetric Fe-terminated slab of 12 Fe-layers and 6 O_3-layers, i.e., the same size as the R$\bar{3}c$ unit cell, and with a 25 Å vacuum layer between the periodic images of the slabs (30 atoms). The anti-ferromagnetic ground state of α-Fe_2O_3 was imposed and verified in all the relaxed structures. The initial GO model comprised a 2×2 graphene cell with a single epoxy group (C:O ratio of 8:1) which could form a bridging oxide ion to Fe on the surface of the stoichiometric α-Fe_2O_3 slab in the composite model. N-doped GO models were constructed by graphitic substitution (C:O:N ratio 7:1:1) and with three pyridinic N adjacent to a C vacancy (C:O:N ratio 7:1:0.75). The latter required a $2 \times 2 \times 1$ supercell due to the size of the dopant cluster. Several configurations were considered for the GO models and composites, and the most important energetics and structural relaxations are presented in the results.

The composite cell was fixed to the relaxed α-Fe_2O_3 lattice parameter, which corresponded to GO being strained relative to the α-Fe_2O_3 material. The optimized lateral lattice parameter of α-Fe_2O_3 was 5.075 Å, in good agreement with previous studies [51,52]. The atomic positions were fixed for two Fe-layers and two O_3-layers in the middle of the slab to ease the relaxation, particularly for the composite slabs. The binding energy, ΔE_b, between the α-Fe_2O_3 slab and GO was calculated from the total energies of the respective cells according to

$$\Delta E_b = \frac{1}{2}\left(E^{tot}_{Fe_2O_3-GO} - E^{tot}_{Fe_2O_3} - 2E^{tot}_{GO}\right) \quad (1)$$

The reference state for the GO models, E^{tot}_{GO}, was taken as the unstrained cells, and ΔE_b thereby includes the energy penalty of straining the GO cells to match the lattice parameter of α-Fe_2O_3. Adsorption of H_2O was considered in symmetric $2 \times 2 \times 1$ α-Fe_2O_3 slabs with both GO and adsorbates on both sides of the slabs (190–192 atoms w/o H_2O). The adsorption energies were calculated according to

$$\Delta E_{ads} = \frac{1}{2}\left(E^{tot}_{H_2O_{ads}} - 2E^{tot}_{H_2O}\right) \quad (2)$$

where $E^{tot}_{H_2O_{ads}}$ is the total energy of the composite with H_2O adsorbates. These calculations were performed using a $2 \times 2 \times 1$ k-point grid. Selected calculations showed that the resulting ΔE_{ads} was within 26 meV of the value obtained with a $4 \times 4 \times 1$ grid. Selected calculations were also performed with the RPBE [53] and PBEsol [54] functionals combined with the D3 dispersion correction scheme [55]. The calculated adsorption energy for the most stable configuration on the Fe_2O_3-GO composite, −1.39 eV (ortho position, see Table 3), was similar to the −1.33 eV adsorption energy obtained with the RPBE functional, which is optimized for gas adsorption. On the other hand, the PBEsol functional which is optimized for solids resulted in a somewhat more exothermic and presumably less correct adsorption enthalpy of −1.58 eV.

3. Results and discussion

3.1. Atomistic structure and GO configurations

The relaxed structures of the GO and N-doped GO models are shown in Fig. 1. The GO cell (2×2 graphene), corresponding to one α-Fe_2O_3 unit cell, is highlighted in Fig. 1a. For the N-doped configurations, the epoxy site was conserved so that it could form the bridging bond to the surface Fe in the composites. Graphitic N was considered at the two symmetrically inequivalent sites, and the alternate site marked in Fig. 1b was less stable by 0.26 eV. There was only one symmetrically inequivalent configuration for three pyridinic N surrounding a carbon vacancy within the initial GO model (Fig. 1c), and this model was constructed in a 4×4 graphene cell. Fig. 2 shows the α-Fe_2O_3 surface unit cell with an undercoordinated Fe coinciding with the epoxy groups in Fig. 1.

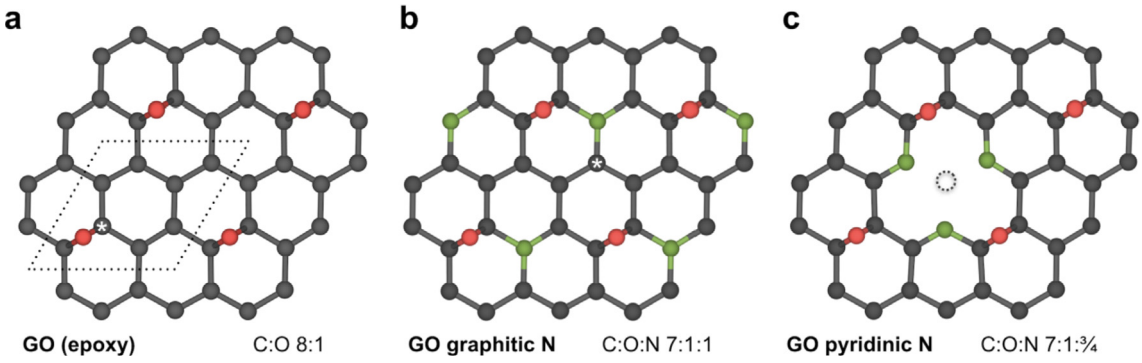

Fig. 1. Relaxed structure of GO with epoxy groups (a), and additional graphitic nitrogen (b), and three pyridinic nitrogen surrounding a carbon vacancy (c). (A colour version of this figure can be viewed online.)

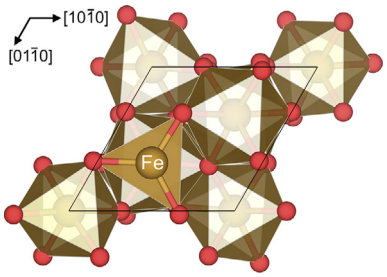

Fig. 2. Relaxed structure of the α-Fe_2O_3 (0 0 0 1) surface showing the undercoordinated iron. (A colour version of this figure can be viewed online.)

The optimized structures of the composite models are shown in Fig. 3. The bridging Fe—O—C bond shown in the figures was found to be slightly more stable than a bridging epoxy group by 1.7 meV. The most stable configuration was used further, and the C—O site is highlighted in Fig. 1a.

Selected structural parameters for the composites are summarized in Table 1. The tensile strain of GO in the composites was about −2% to −3%, i.e., quite low compared to other composite structures. The surface rumpling in the GO layer occurred exclusively at the bridging bond and it was lower for the composites than for the corresponding epoxy GO structures in Fig. 1. The Fe—O bond length was about 1.9 Å in all cases, which lies between the surface Fe—O bond length, 1.81 Å, and the bulk values, 1.95—2.14 Å. The C—O bond length in graphitic N-doped GO, 1.34 Å, was shorter than for GO and pyridinic N-doped GO, 1.40—1.41 Å.

The binding energies of the composites were found to be exothermic for all the GO models, ranging from −0.56 eV to −1.14 eV per α-Fe_2O_3 cell or Fe—O bond (Table 1). These values imply strong chemical bonding between the materials and that the composites are robust and thermally stable.

3.2. Electronic structure and Bader charge analysis

The calculated band gaps of α-Fe_2O_3 were 2.26 eV for bulk and 2.21 eV for the (0 0 0 1) surface slab which are in good agreement with previous theoretical studies [41,43] and experimental values for the optical gap, 2.0—2.2 eV [56]. The electronic density of states of the isolated materials and composites are shown in Fig. 4, and the α-Fe_2O_3 (0 0 0 1) band gap is highlighted as a gray region in the bottom panels. The gap states at around 1.8 eV were mainly associated with the d_{z^2} orbital of the surface Fe ion, and these states disappeared in the composites as the bridging Fe—O—C bond was formed. The O 2p states extending beyond the valence band edge were associated with the surface oxide ions and the apparent extension of the conduction band into the band gap was attributed to the 0.1 eV Gaussian smearing.

The composites exhibited partly occupied carbon states above the α-Fe_2O_3 valence band maximum (VBM). In the case of undoped GO, the Fermi level was 0.16 eV above VBM, and 0.14 eV above VBM in the composite (Fig. 4a). The Fermi level in graphitic N-doped GO was 0.64 eV above VBM, which can be ascribed to n-type doping due to the excess electron when nitrogen substitutes for carbon (Fig. 4b) [57]. The corresponding composite showed carbon and nitrogen states below the conduction band and fewer carbon states above VBM compared to Fe_2O_3-GO. Pyridinic N-doped GO showed more localized N-states below VBM and the Fermi level was 0.02 eV below VBM. The electronic structure of the composite was similar to that of Fe_2O_3-GO albeit with occupied N-states close to VBM (Fig. 4c).

Bader charge analysis revealed that the oxygen in the epoxy groups attained a higher negative charge with increasing Fermi level in the GO structures (Table 2). Furthermore, the bridging oxide ion in the composites exhibited a higher negative charge than the epoxy group in the corresponding isolated GO structures. On the other hand, the charge of the bridging Fe ion remained unchanged and identical to bulk ($Fe^{1.8+}$). The higher negative charge of the bridging oxide ion may be attributed to a more ionic Fe—O—C bond relative to the covalent epoxy group, perhaps promoted by charge transfer from GO due to the higher Fermi level, at least in the case of GO and graphitic N-doped GO (Fig. 4). The charge of the bridging oxide ion was found to correlate well with the binding energies in Table 1, indicating a stronger Fe—O—C bond with increasing negative charge of the oxide ion. The charge of nitrogen in the composites amounted to $N^{2.1-}$ and $N^{2.9-}$ for graphitic and pyridinic nitrogen, respectively.

3.3. Adsorption of H_2O

On the α-Fe_2O_3 (0 0 0 1) surface, water dissociatively adsorbs as a hydroxide species bound to the undercoordinated Fe (see Fig. 2) and a proton associated with a surface oxide ion with an adsorption energy of about −1 eV [52,58]. In the nanocomposites, the surface Fe was fully coordinated due to the bridging Fe—O—C bond. Dissociative adsorption of H_2O was therefore considered with hydroxide adsorbed to the GO part of the composite, and the proton associated with the surface oxide ion of α-Fe_2O_3, unless otherwise stated. The adsorption site for the hydroxide species was considered for symmetrically inequivalent carbon sites. Based on initial calculations, it was determined that it was not favorable for hydroxide to adsorb and bond to nitrogen sites or the nearest

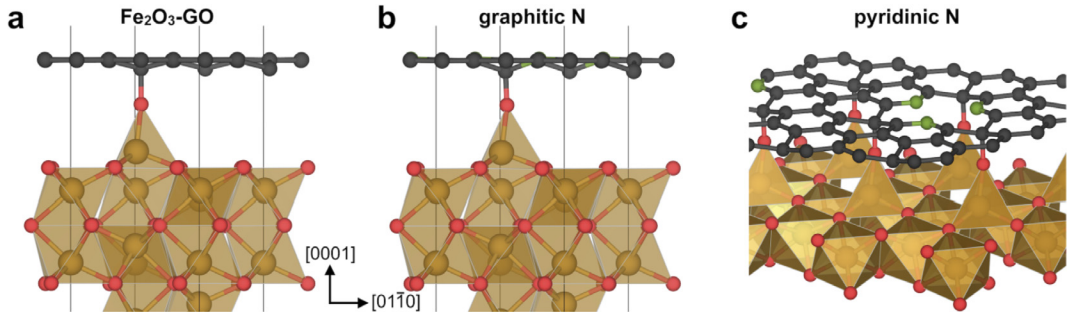

Fig. 3. Relaxed structure of the Fe_2O_3-GO composite (a), with graphitic N-doping (b) and with pyridinic N-doping (c). The first two figures show half of the α-Fe_2O_3 unit cell along the c-direction, while the latter shows the surface layer of a 2×2 α-Fe_2O_3 cell. (A colour version of this figure can be viewed online.)

Table 1
Structural parameters for the Fe_2O_3-GO composites with values in parenthesis for the free-standing GO structures, and binding energy between α-Fe_2O_3 and GO, ΔE_b, per Fe–O–C bond or α-Fe_2O_3 unit cell.

	GO	GO graphitic N	GO pyridinic N
Strain/%	−1.95	−2.96	−1.82
Rumpling/Å	0.33 (0.21)	0.42 (0.27)	0.33 (0.25)
C–O/Å	1.41	1.34	1.40
Fe–O/Å	1.89	1.90	1.89
ΔE_b/eV	−0.56	−1.14	−0.84

Table 2
Bader charge of oxygen in the epoxy groups in isolated (N-doped) GO and in the Fe–O–C bridge in the composites.

Material	Oxygen charge	
	Epoxy	Fe–O–C
GO	−1.1	−1.3
GO graphitic N	−1.2	−1.7
GO pyridinic N	−1.0	−1.4

neighboring carbon site. The most stable adsorption configurations with a α-Fe_2O_3 surface proton and hydroxide adsorbed to (N-doped) GO are shown in Fig. 5. Adsorption of hydroxide resulted in outward relaxation of carbon by 0.37–0.43 Å and the C–OH bond lengths were 1.45–1.48 Å.

The obtained adsorption energies are summarized in Table 3 where the OH position is denoted in relation to the carbon in the Fe–O–C bridge as shown in Fig. 5. The adsorption energies with hydroxide in the ortho and para positions were the most favorable, in agreement with hydroxide adsorption on pristine graphene [59]. In the case of the N-doped GO composites, the ortho configurations were most favorable. Notably, all of the nanocomposites exhibit more exothermic adsorption energies than the individual materials.

In the case of the Fe_2O_3-GO, a more stable configuration was obtained with the hydroxide group residing between GO and the α-Fe_2O_3 surface (Fig. 6a). This configuration allowed for an additional hydrogen bond between hydroxide and the Fe–O–C bridge that can explain the more exothermic adsorption energy of −1.39 eV (Table 3). In the case of pyridinic N-doped GO, the most stable configuration, with an adsorption energy of −1.66 eV, was obtained by forming an NH group instead of the α-Fe_2O_3 surface proton, as shown in Fig. 6b. Adsorption to NH was also achieved by retaining the α-Fe_2O_3 surface proton and changing ortho hydroxide to ortho carbonyl, resulting in an adsorption energy of −1.47 eV. However, the formation of two NH groups in the same pyridinic unit was significantly less favorable. Based on the adsorption energies of these configurations, the binding energy of the proton in the NH group was −0.32 eV relative to the α-Fe_2O_3 surface proton, and −0.19 eV relative to the proton in the ortho hydroxide group.

In terms of functional properties and catalytic activity, the large

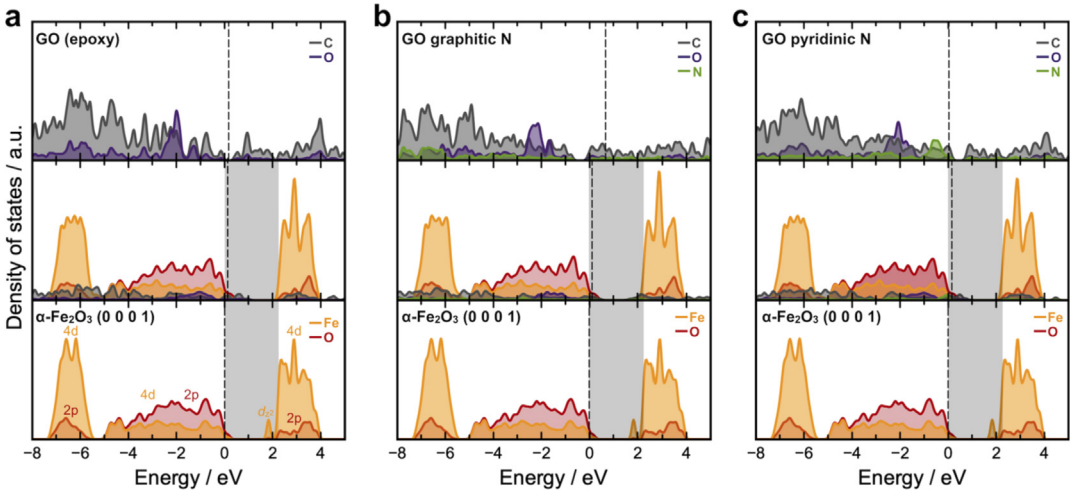

Fig. 4. Electronic density of states for the isolated materials and composite for Fe_2O_3-GO (a), with graphitic N-doping (b) and with pyridinic N-doping (c). The dashed lines represent the highest (partially) occupied states. The valence band maximum of α-Fe_2O_3 (0 0 0 1) was referenced to 0 eV. The composite and GO cells were aligned by deep Fe 3p states and the potential in the vacuum region, respectively. (A colour version of this figure can be viewed online.)

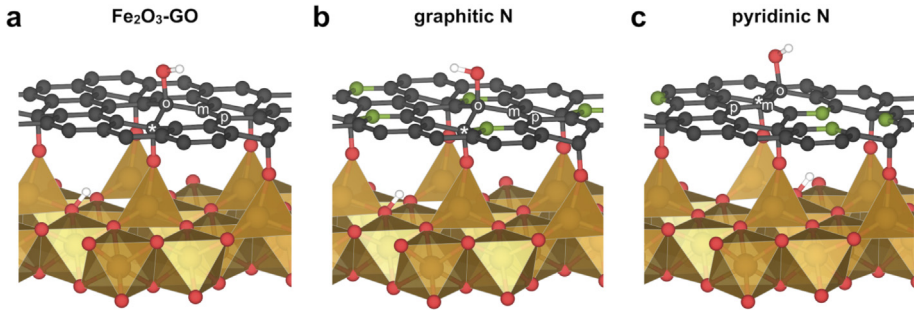

Fig. 5. Most stable configurations of dissociatively adsorbed H_2O with the hydroxide on the ortho site in GO and the proton associated with the α-Fe_2O_3 surface oxide ion for Fe_2O_3-GO (a), with graphitic N-doping (b) and with pyridinic N-doping (c). (A colour version of this figure can be viewed online.)

Table 3
Adsorption energy for dissociative chemisorption of H_2O with a proton bound to a α-Fe_2O_3 surface oxide ion and hydroxide bound to GO positions relative to the Fe–O–C bridge as defined in Fig. 5. Additional configurations are described in Fig. 6.

OH site	H_2O adsorption energy/eV		
	GO	GO graphitic N	GO pyridinic N
Ortho	−1.39	−1.50	−1.34/−1.66
Meta	−0.14	0.42	0.40
Para	−1.00/−1.39	−0.94	−1.08

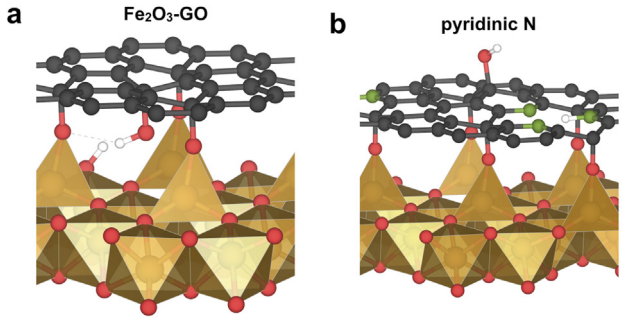

Fig. 6. Dissociatively adsorbed H_2O on Fe_2O_3-GO with para hydroxide in between GO and the α-Fe_2O_3 (0001) surface forming a hydrogen bond with the Fe–O–C bridge (a), and pyridinic N-doped GO with ortho hydroxide and one NH group (b). (A colour version of this figure can be viewed online.)

negative chemisorption energies imply that the nanocomposite may be significantly affected – structurally and chemically – by the presence of H_2O. In an aqueous environment, the nanocomposites may become permanently modified by chemisorption in the most stable configurations, while other parts of the composites provide the active sites for reactions such as water splitting.

4. Conclusion

Graphene oxide and α-Fe_2O_3 may form robust nanocomposites due to strong Fe–O–C bonds bridging the materials. The calculated binding energies between the materials ranged from −0.56 eV to −1.14 eV per Fe–O–C bond despite the penalty of inducing tensile strain in the GO part of the computational cells. The exothermicity of the binding energy was found to correlate with a more negative charge of the bridging oxide ion. Dissociative adsorption of H_2O was determined to be more exothermic for the nanocomposites than the isolated materials since the dissociated species – hydroxide and proton – could adsorb to different parts of the composite. Hydroxide species were found to preferentially adsorb on the ortho position in (N-doped) GO relative to the Fe–O–C bridge, while protons were most stable associated with an oxide ion on the α-Fe_2O_3 surface or as an NH group in the case of the composite with pyridinic N-doped GO. The resulting adsorption energies were about −0.9 eV to −1.7 eV per H_2O for the most stable configurations, which implies that the nanocomposites may be significantly modified due to chemisorption in an aqueous environment.

Acknowledgements

The authors acknowledge financial support from the Research Council of Norway through 2Defect (262274) and PhotoNGrapHy (246809) under the FRIPRO and ENERGIX programs, respectively. The computations were performed on resources provided by UNINETT Sigma2 – the National Infrastructure for High Performance Computing and Data Storage in Norway – under the project NN9259K.

References

[1] X. Li, J. Yu, S. Wageh, A.A. Al-Ghamdi, J. Xie, Graphene in photocatalysis: a review, Small 12 (2016) 6640–6696, https://doi.org/10.1002/smll.201600382.
[2] R.K. Upadhyay, N. Soin, S.S. Roy, Role of graphene/metal oxide composites as photocatalysts, adsorbents and disinfectants in water treatment: a review, RSC Adv. 4 (2014) 3823–3851, https://doi.org/10.1039/c3ra45013a.
[3] M.F. El-Kady, Y. Shao, R.B. Kaner, Graphene for batteries, supercapacitors and beyond, Nat. Rev. Mater. 1 (2016) 1–14, https://doi.org/10.1038/natrevmats.2016.33.
[4] S. Gupta Chatterjee, S. Chatterjee, A.K. Ray, A.K. Chakraborty, Graphene-metal oxide nanohybrids for toxic gas sensor: a review, Sensor. Actuator. B Chem. 221 (2015) 1170–1181, https://doi.org/10.1016/j.snb.2015.07.070.
[5] L.K. Putri, W.J. Ong, W.S. Chang, S.P. Chai, Heteroatom doped graphene in photocatalysis: a review, Appl. Surf. Sci. 358 (2015) 2–14, https://doi.org/10.1016/j.apsusc.2015.08.177.
[6] Q. Xiang, B. Cheng, J. Yu, Graphene-based photocatalysts for solar-fuel generation, Angew. Chem. 54 (2015) 11350–11366, https://doi.org/10.1002/anie.201411096.
[7] J. Kusuma, R.G. Balakrishna, S. Patil, M.S. Jyothi, H.R. Chandan, R. Shwetharani, Exploration of graphene oxide nanoribbons as excellent electron conducting network for third generation solar cells, Sol. Energy Mater. Sol. Cells 183 (2018) 211–219, https://doi.org/10.1016/j.solmat.2018.01.039.
[8] Z.S. Wu, W. Ren, D.W. Wang, F. Li, B. Liu, H.M. Cheng, High-energy MnO_2 nanowire/graphene and graphene asymmetric electrochemical capacitors, ACS Nano 4 (2010) 5835–5842, https://doi.org/10.1021/nn101754k.
[9] F. Bonaccorso, L. Colombo, G. Yu, M. Stoller, V. Tozzini, A.C. Ferrari, R.S. Ruoff, V. Pellegrini, Graphene, related two-dimensional crystals, and hybrid systems for energy conversion and storage, Science 347 (2015) 41, https://doi.org/10.1126/science.1246501.
[10] S. Mallick, P.P. Jana, C.R. Raj, Asymmetric supercapacitor based on chemically coupled hybrid material of Fe_2O_3-Fe_3O_4 heterostructure and nitrogen-doped reduced graphene oxide, ChemElectroChem 5 (2018) 2348–2356, https://doi.org/10.1002/celc.201800521.
[11] W. Ma, S. Chen, S. Yang, W. Chen, W. Weng, Y. Cheng, M. Zhu, Flexible all-solid-state asymmetric supercapacitor based on transition metal oxide nanorods/reduced graphene oxide hybrid fibers with high energy density, Carbon 113 (2017) 151–158, https://doi.org/10.1016/j.carbon.2016.11.051.
[12] F.K. Meng, J.T. Li, S.K. Cushing, J. Bright, M.J. Zhi, J.D. Rowley, Z.L. Hong, A. Manivannan, A.D. Bristow, N.Q. Wu, Photocatalytic water oxidation by

hematite/reduced graphene oxide composites, ACS Catal. 3 (2013) 746–751, https://doi.org/10.1021/Cs300740e.
[13] Y. Gao, D. Wu, T. Wang, D. Jia, W. Xia, Y. Lv, Y. Cao, Y. Tan, P. Liu, One-step solvothermal synthesis of quasi-hexagonal Fe_2O_3 nanoplates/graphene composite as high performance electrode material for supercapacitor, Electrochim. Acta 191 (2016) 275–283, https://doi.org/10.1016/j.electacta.2016.01.072.
[14] Y. Zhu, S. Cheng, W. Zhou, J. Jia, L. Yang, M. Yao, M. Wang, J. Zhou, P. Wu, M. Liu, Construction and performance characterization of α-Fe_2O_3/rGO composite for long-cycling-life supercapacitor anode, ACS Sustain. Chem. Eng. 5 (2017) 5067–5074, https://doi.org/10.1021/acssuschemeng.7b00445.
[15] D. Wu, P. Liu, T. Wang, X. Chen, L. Yang, D. Jia, Amino acid-assisted synthesis of Fe_2O_3/nitrogen doped graphene hydrogels as high performance electrode material, Electrochim. Acta 283 (2018) 1858–1870, https://doi.org/10.1016/j.electacta.2018.07.103.
[16] Y. Wang, M. Zhang, D. Pan, Y. Li, T. Ma, J. Xie, Nitrogen/sulfur co-doped graphene networks uniformly coupled N-Fe_2O_3 nanoparticles achieving enhanced supercapacitor performance, Electrochim. Acta 266 (2018) 242–253, https://doi.org/10.1016/j.electacta.2018.02.040.
[17] Y. Dong, X. Zhang, X. Cheng, Y. Xu, S. Gao, H. Zhao, L. Huo, Highly selective NO_2 sensor at room temperature based on nanocomposites of hierarchical nanosphere-like α-Fe_2O_3 and reduced graphene oxide, RSC Adv. 4 (2014) 57493–57500, https://doi.org/10.1039/C4RA10136G.
[18] M.Y. Wang, T. Shen, M. Wang, D.E. Zhang, Z.W. Tong, J. Chen, One-pot synthesis of α-Fe_2O_3 nanoparticles-decorated reduced graphene oxide for efficient nonenzymatic H_2O_2 biosensor, Sensor. Actuator. B Chem. 190 (2014) 645–650, https://doi.org/10.1016/j.snb.2013.08.091.
[19] V. Blechta, M. Mergl, K. Drogowska, V. Valeš, M. Kalbáč, NO_2 sensor with a graphite nanopowder working electrode, Sensor. Actuator. B Chem. 226 (2016) 299–304, https://doi.org/10.1016/j.snb.2015.11.130.
[20] X. Jia, D. Lian, B. Shi, R. Dai, C. Li, X. Wu, Facile synthesis of α-Fe_2O_3@graphene oxide nanocomposites for enhanced gas-sensing performance to ethanol, J. Mater. Sci. Mater. Electron. 28 (2017) 12070–12079, https://doi.org/10.1007/s10854-017-7019-y.
[21] W. Zhou, J. Zhu, C. Cheng, J. Liu, H. Yang, C. Cong, C. Guan, X. Jia, H.J. Fan, Q. Yan, C.M. Li, T. Yu, A general strategy toward graphene@metal oxide core-shell nanostructures for high-performance lithium storage, Energy Environ. Sci. 4 (2011) 4954–4961, https://doi.org/10.1039/c1ee02168k.
[22] H. Li, L. Xu, H. Sitinamaluwa, K. Wasalathilake, C. Yan, Coating Fe_2O_3 with graphene oxide for high-performance sodium-ion battery anode, Compos. Commun. 1 (2016) 48–53, https://doi.org/10.1016/j.coco.2016.09.004.
[23] H.-J. Song, X.-H. Jia, N. Li, X.-F. Yang, H. Tang, Synthesis of α-Fe_2O_3 nanorod/graphene oxide composites and their tribological properties, J. Mater. Chem. 22 (2012) 895, https://doi.org/10.1039/c1jm13740a.
[24] S. Mao, H. Pu, J. Chen, Graphene oxide and its reduction: modeling and experimental progress, RSC Adv. 2 (2012) 2643, https://doi.org/10.1039/c2ra00663d.
[25] D. D'Angelo, C. Bongiorno, M. Amato, I. Deretzis, A. La Magna, G. Compagnini, S.F. Spanò, S. Scalese, Electron energy-loss spectra of graphene oxide for the determination of oxygen functionalities, Carbon 93 (2015) 1034–1041, https://doi.org/10.1016/j.carbon.2015.06.025.
[26] S. Pei, H.-M. Cheng, The reduction of graphene oxide, Carbon 50 (2012) 3210–3228, https://doi.org/10.1016/j.carbon.2011.11.010.
[27] A.L.M. Reddy, A. Srivastava, S.R. Gowda, H. Gullapalli, M. Dubey, P.M. Ajayan, Synthesis of nitrogen-doped graphene films for lithium battery application, ACS Nano 4 (2010) 6337–6342, https://doi.org/10.1021/nn101926g.
[28] H. Wang, T. Maiyalagan, X. Wang, Review on recent progress in nitrogen-doped graphene: synthesis, characterization, and its potential applications, ACS Catal. 2 (2012) 781–794, https://doi.org/10.1021/cs200652y.
[29] J.M. Polfus, T.S. Bjørheim, T. Norby, R. Haugsrud, Nitrogen defects in wide band gap oxides: defect equilibria and electronic structure from first principles calculations, Phys. Chem. Chem. Phys. 14 (2012) 11808–11815, https://doi.org/10.1039/c2cp41378g.
[30] M.T. Nguyen, R. Gebauer, Graphene supported on hematite surfaces: a density functional study, J. Phys. Chem. C 118 (2014) 8455–8461, https://doi.org/10.1021/jp501171t.
[31] P.N.O. Gillespie, N. Martsinovich, Electronic structure and charge transfer in the TiO_2 rutile (110)/graphene composite using hybrid DFT calculations, J. Phys. Chem. C 121 (2017) 4158–4171, https://doi.org/10.1021/acs.jpcc.6b12506.
[32] S.B. Cho, Y.-C. Chung, Spin-polarized bandgap of graphene induced by alternative chemisorption with MgO (111) substrate, Carbon 77 (2014) 208–214, https://doi.org/10.1016/j.carbon.2014.05.023.
[33] F. Opoku, K. Kuben, C. Gertina, C. Elizabeth, V. Sittert, P. Poomani, Tuning the electronic structures , work functions , optical property and stability of bifunctional hybrid graphene oxide/V-doped $NaNbO_3$ type-II heterostructures : a promising photocatalyst for H_2 production, Carbon 136 (2018) 187–195, https://doi.org/10.1016/j.carbon.2018.04.076.
[34] P. Zhang, Y. Shen, W. Wu, J. Li, Z. Zhou, Enhanced photocatalytic performance of $KNbO_3$(100)/reduced graphene oxide nanocomposites investigated using first-principles calculations: RGO reductivity effect, Appl. Surf. Sci. 434 (2018) 932–939, https://doi.org/10.1016/j.apsusc.2017.10.239.
[35] J.M. Polfus, O.M. Løvvik, P.M. Rørvik, R. Bredesen, Nanocomposites of few-layer graphene oxide and alumina by density functional theory calculations, J. Eur. Ceram. Soc. 36 (2016) 719–724, https://doi.org/10.1016/j.jeurceramsoc.2015.11.009.
[36] S. Umrao, S. Abraham, F. Theil, S. Pandey, V. Ciobota, P.K. Shukla, C.J. Rupp, S. Chakraborty, R. Ahuja, J. Popp, B. Dietzek, A. Srivastava, A possible mechanism for the emergence of an additional band gap due to a Ti-O-C bond in the TiO_2-graphene hybrid system for enhanced photodegradation of methylene blue under visible light, RSC Adv. 4 (2014) 59890–59901, https://doi.org/10.1039/c4ra10572a.
[37] G. Kresse, D. Joubert, From ultrasoft pseudopotentials to the projector augmented-wave method, Phys. Rev. B 59 (1999) 1758–1775, https://doi.org/10.1103/PhysRevB.59.1758.
[38] P.E. Blöchl, Projector augmented-wave method, Phys. Rev. B 50 (1994) 17953–17979, https://doi.org/10.1103/PhysRevB.50.17953.
[39] J. Perdew, K. Burke, M. Ernzerhof, Generalized gradient approximation made simple, Phys. Rev. Lett. 77 (1996) 3865–3868, https://doi.org/10.1103/PhysRevLett.77.3865.
[40] S.L. Dudarev, S.Y. Savrasov, C.J. Humphreys, A.P. Sutton, Electron-energy-loss spectra and the structural stability of nickel oxide: An LSDA+U study, Phys. Rev. B 57 (1998) 1505–1509, https://doi.org/10.1103/PhysRevB.57.1505.
[41] P. Liao, E. a Carter, Testing variations of the GW approximation on strongly correlated transition metal oxides: hematite (α-Fe_2O_3) as a benchmark, Phys. Chem. Chem. Phys. 13 (2011) 15189–15199, https://doi.org/10.1039/c1cp20829b.
[42] M.C. Toroker, Theoretical insights into the mechanism of water oxidation on nonstoichiometric and titanium-doped Fe_2O_3 (0001), J. Phys. Chem. C 118 (2014) 23162–23167, https://doi.org/10.1021/jp5073654.
[43] O. Neufeld, M. Caspary Toroker, Platinum-doped α-Fe_2O_3 for enhanced water splitting efficiency: a DFT+U study, J. Phys. Chem. C 119 (2015) 5836–5847, https://doi.org/10.1021/jp512002f.
[44] S. Grimme, Semiempirical GGA-type density functional constructed with a long-range dispersion correction, J. Comput. Chem. 16 (2006) 1787–1799, https://doi.org/10.1002/jcc.
[45] G. Mercurio, E.R. McNellis, I. Martin, S. Hagen, F. Leyssner, S. Soubatch, J. Meyer, M. Wolf, P. Tegeder, F.S. Tautz, K. Reuter, Structure and energetics of azobenzene on Ag(111): benchmarking semiempirical dispersion correction approaches, Phys. Rev. Lett. 104 (2010), 036102, https://doi.org/10.1103/PhysRevLett.104.036102.
[46] D. Stradi, S. Barja, C. Díaz, M. Garnica, B. Borca, J.J. Hinarejos, D. Sánchez-Portal, M. Alcamí, A. Arnau, A.L. Vázquez de Parga, R. Miranda, F. Martín, Role of dispersion forces in the structure of graphene monolayers on Ru surfaces, Phys. Rev. Lett. 106 (2011) 186102, https://doi.org/10.1103/PhysRevLett.106.186102.
[47] B. Huang, Q. Xu, S.-H. Wei, Theoretical study of corundum as an ideal gate dielectric material for graphene transistors, Phys. Rev. B 84 (2011) 155406, https://doi.org/10.1103/PhysRevB.84.155406.
[48] S. Cho, S. Lee, Y. Chung, Water trapping at the graphene/Al_2O_3 interface, Jpn. J. Appl. Phys. 52 (2013), 06GD09. https://doi.org/10.7567/JJAP.52.06GD09.
[49] S.B. Cho, Y.-C. Chung, Bandgap engineering of graphene by corrugation on lattice-mismatched MgO (111), J. Mater. Chem. C. 1 (2013) 1595, https://doi.org/10.1039/c2tc00257d.
[50] X.F. Fan, W.T. Zheng, V. Chihaia, Z.X. Shen, J.-L. Kuo, Interaction between graphene and the surface of SiO_2, J. Phys. Condens. Matter 24 (2012) 305004, https://doi.org/10.1088/0953-8984/24/30/305004.
[51] M.-T. Nguyen, N. Seriani, S. Piccinin, R. Gebauer, Photo-driven oxidation of water on α-Fe_2O_3 surfaces: an ab initio study, J. Chem. Phys. 140 (2014), 064703, https://doi.org/10.1063/1.4865103.
[52] R.B. Wang, A. Hellman, Initial water adsorption on hematite (α -Fe_2O_3) (0001): a DFT + U study, J. Chem. Phys. 148 (2018), 094705, https://doi.org/10.1063/1.5020358.
[53] B. Hammer, L.B. Hansen, J.K. Nørskov, Improved adsorption energetics within density-functional theory using revised Perdew-Burke-Ernzerhof functionals, Phys. Rev. B - Condens. Matter Mater. Phys. 59 (1999) 7413, https://doi.org/10.1103/PhysRevB.59.7413.
[54] G.I. Csonka, J.P. Perdew, A. Ruzsinszky, P.H.T. Philipsen, S. Lebègue, J. Paier, O.A. Vydrov, J.G. Ángyán, Assessing the performance of recent density functionals for bulk solids, Phys. Rev. B - Condens. Matter Mater. Phys. 79 (2009) 155107, https://doi.org/10.1103/PhysRevB.79.155107.
[55] S. Grimme, J. Antony, S. Ehrlich, H. Krieg, A consistent and accurate ab initio parametrization of density functional dispersion correction (DFT-D) for the 94 elements H-Pu, J. Chem. Phys. 132 (2010) 154104, https://doi.org/10.1063/1.3382344.
[56] P. Merchant, R. Collins, R. Kershaw, K. Dwight, A. Wold, The electrical, optical and photoconducting properties of $Fe_{2-x}Cr_xO_3$($0 \leq x \leq 0.47$), J. Solid State Chem. 27 (1979) 307–315, https://doi.org/10.1016/0022-4596(79)90173-7.
[57] F. Joucken, Y. Tison, P. Le Fèvre, A. Tejeda, A. Taleb-Ibrahimi, E. Conrad, V. Repain, C. Chacon, A. Bellec, Y. Girard, S. Rousset, J. Ghijsen, R. Sporken, H. Amara, F. Ducastelle, J. Lagoute, Charge transfer and electronic doping in nitrogen-doped graphene, Sci. Rep. 5 (2015) 14564, https://doi.org/10.1038/srep14564.
[58] M. Nguyen, N. Seriani, R. Gebauer, M. Nguyen, N. Seriani, R. Gebauer, Water adsorption and dissociation on α-Fe_2O_3 (0001): PBE+U calculations, J. Chem. Phys. 3 (2015) 1–8, https://doi.org/10.1063/1.4804999.
[59] N. Ghaderi, M. Peressi, First-principle study of hydroxyl functional groups on pristine, defected graphene, and graphene epoxide, J. Phys. Chem. C 114 (2010) 21625–21630, https://doi.org/10.1021/jp108688m.